Creating Virtual Skies

First Year PhD Transfer Report

Michael Peel

Supervisors: Prof. Ian Browne & Dr. Richard Battye

Jodrell Bank Centre for Astrophysics
Department of Physics and Astronomy
The University of Manchester

31 May 2007

Abstract
The Sunyaev-Zel'dovich effect in clusters of galaxies presents a unique and independent cosmological probe. However, contamination, confusion and noise in the detections of clusters needs to be quantified and corrected for before reliable cosmological measurements can be extracted. Here, the creation of virtual sky maps is documented, which consist of the Cosmic Microwave Background, the SZ effect and point sources. This constitutes the first step into an investigation of the methods of carrying out SZ effect detections, as well as ways of counteracting the issues surrounding them.

Contents

1 Introduction

This document records the author's work during the first 8 months of his postgraduate research. The main focus of this work to date has been the construction of a program capable of creating virtual skies at gigahertz frequencies. These consist of the Cosmic Microwave Background (CMB) with modifications by the Sunyaev-Zel'dovich effect arising from clusters of galaxies, as well as a foreground of radio and infrared point sources.

The following section provides a definition of a galaxy cluster and gives an overview of the main methods of observing them. §3 discusses the different components of the virtual sky, starting with the cosmology (the CMB and the distribution of galaxy clusters), followed by a description of the model used for galaxy clusters and concluding with point source contamination. §4 outlines the expected future progression of this work in various directions, and §5 concludes this document. Two appendices are provided; the first gives a description of the pixelization of the sky and the process of convolving a map with a telescope beam, while the second gives an overview of the structure of the virtual sky program.

2 Galaxy clusters

A galaxy cluster is generally defined as a set of over 50 galaxies in close ($\lesssim$ 2Mpc) proximity to each other; sets of galaxies smaller than this are termed "galaxy groups". Pioneering work on the classification of galaxy clusters was done by Abell (1958), leading to the definition of a "richness" factor that depends on the number of constituent galaxies can be allotted to each cluster. Table 1 shows Abell's definition of this factor.

Galaxy clusters emit radiation across the entire electromagnetic spectrum. Optical and infrared observations can locate individual galaxies; however, only about 10% of the baryonic mass of a cluster is contained within the galaxies. The rest forms the IntraCluster Medium (ICM; also known as the intergalactic medium or the intracluster plasma). The majority of this is hot gas located in the center of the cluster, where it is heated predominantly by energy from the infall of matter into the cluster's gravitational well (although other effects also provide sources of energy). Due to its temperature, it emits thermal radiation as X-rays, and it can also be observed via its effect on photons from the CMB. It has cosmological importance as it provides a tracer for locating clusters of galaxies, the distribution of which can provide constraints on fundamental cosmological parameters.

The baryonic mass of the cluster only makes up around a seventh of its total mass (Ostriker et al., 2005). The remainder consists of dark matter, probably in the form of a cluster halo and a series of sub-haloes, which are most likely associated with individual galaxies. The presence of this dark matter can be inferred both from the application of the virial theorem to the motions of galaxies within the cluster as well as gravitational lensing. Its distribution can potentially be related to the distribution of galaxies (and hence radio sources) within the cluster.

Richness class	Galaxy counts
0	30–49
1	50–79
2	80–129
3	130–199
4	200–299
5	300 or over

Table 1: Richness classes, as defined by Abell (1958).

2.1 Optical and infrared observations

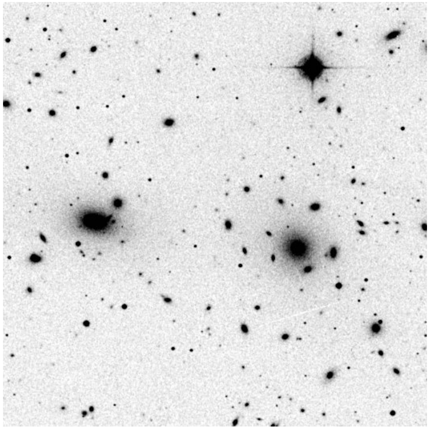

Figure 1: The Coma Cluster (Abell 1656) at 645nm. From the *Digitized Sky Survey*.

Clusters of galaxies have been identified using optical wavelengths since the late 18th century (see Biviano, 2000, for a historical review). The standard catalogue for the subject is that published by Abell (1958) (also Abell et al., 1989), which focuses on clusters with more than 50 component galaxies that are fairly close to our galaxy, i.e. with redshifts up to $z \approx 0.2$.

Optical observations show that there is frequently a Brightest Cluster Galaxy (BCG) or a first-ranked galaxy at the centre of galaxy clusters. These massive, luminous galaxies only appear in clusters—never in the field—and are mostly evolved and elliptical. Around 20% are surrounded by a low surface brightness envelope; these are also called cD galaxies. (Oegerle & Hill, 2001; Seigar et al., 2006).

Cluster galaxies can also be split up into several groups depending on their positions on a colour–magnitude diagram; these groups are normally the red and blue sequences. The red galaxies in the cluster are old and passively evolving, and form a tight sequence in colour–magnitude diagrams (De Lucia et al., 2004). They can be used to locate clusters (e.g. the Red-Sequence Cluster Survey, Gladders & Yee, 2000).

Spectroscopy forms an important part of the optical observations of galaxies in clusters, as it allows the redshifts of the clusters to be measured to high precision ($\Delta z \sim 0.01$), as well as providing measurements of the velocity dispersion of the galaxies. Large-scale surveys aimed at obtaining redshifts for large numbers of galaxies are currently in progress, for example the Sloan Digital Sky Survey (SDSS; York et al., 2000).

Galaxy clusters are complicated, diffuse objects in the optical regime (see Figure 1). It often proves tricky to differentiate between cluster galaxies and foreground galaxies (hence the selection methods used by Abell, 1958). In general, spectroscopic observations of the galaxies are needed to identify their redshifts, so that their line-of-sight distances are known. N-body techniques such as friends-of-friends can also be applied to select the cluster galaxies (Clewley et al., 2006).

2.2 X-ray emission

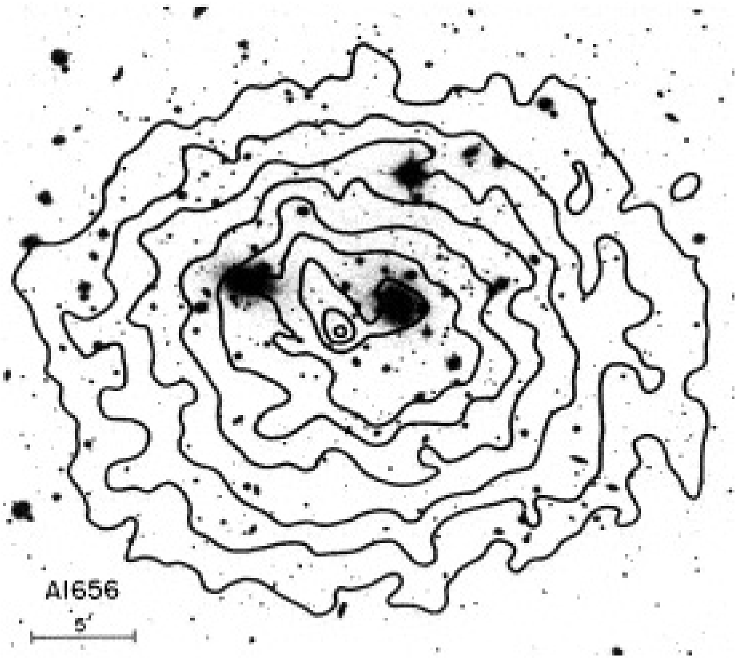

Figure 2: The Coma Cluster (Abell 1656) at 0.15nm (8.0–8.2keV X-rays; contours) overlaid on an optical image of the cluster. From *Einstein* (Jones & Forman, 1999).

Due to the temperature of the gas in the ICM, thermal emission is given off as X-rays mostly via thermal bremsstrahlung, but also through line radiation. The spectral surface brightness at energy E along a particular line of sight l is given by (Birkinshaw, 1999)

$$b(\theta, E) = \frac{1}{4\pi(1+z)^3} \int n_{\mathrm{e}}(\theta)^2 \Lambda(E(\theta), T_{\mathrm{e}}(\theta)) dl, \tag{1}$$

where z is the cluster's redshift, $n_{\mathrm{e}}(\theta)$ is the electron number density at a distance θ from the center of the cluster and $\Lambda(E, T_{\mathrm{e}})$ is the spectral emissivity at X-ray energy $E(\theta)$ of a gas at temperature $T_{\mathrm{e}}(\theta)$; this function is generally complicated. A related parameter is the cooling function, which gives the total energy emitted from a gas at temperature T_{e}.

The intensity of X-rays emitted depends on the square of the electron density, hence X-ray observations predominantly see the cores of the galaxy clusters, rather than the outskirts of the cluster (see Figure 2). The gas in the cluster center can be subject to complicating effects including heating and cooling (see e.g. Motl et al., 2005), and the X-ray emission will also be more sensitive to clumps in the gas.

2.3 The Sunyaev-Zel'dovich effect

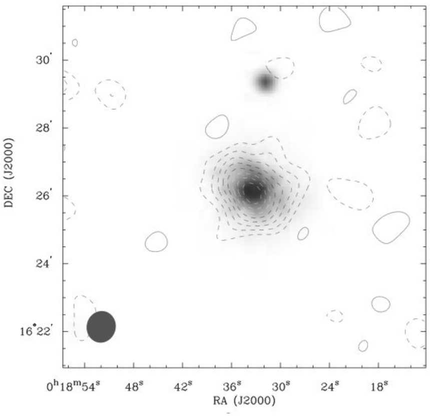

Figure 3: Detection of the SZ effect in CL 0016+16 at 1cm (contours) by the OVRO Millimeter Array superimposed on the X-ray emission from the cluster (grey-scale) by ROSAT (Carlstrom et al., 1996a,b).

The Sunyaev-Zel'dovich (SZ) effect is due to the inverse Compton scattering of photons from the CMB when they pass through the hot electron gas in the ICM. The photons gain energy from the electrons and are hence shifted up in frequency, meaning that the SZ effect is manifested as a decrement in the CMB at low frequencies and an increment at high frequencies, with a null at 217GHz. It was predicted by Sunyaev & Zeldovich (1970, 1972), based on earlier work by Weymann (1966) and Zeldovich & Sunyaev (1969). It can be parameterized by the Compton $y(\theta)$ parameter, which represents the integrated pressure along the line of sight l at a distance θ from the center of the cluster, by (Birkinshaw, 1999)

$$y(\theta) = \frac{\sigma_{\mathrm{T}} k_{\mathrm{B}}}{m_{\mathrm{e}} c^2} \int n_{\mathrm{e}}(\theta) T_{\mathrm{e}}(\theta)\ dl, \tag{2}$$

where σ_{T} is the Thomson scattering cross-section, k_{B} is Boltzmann's constant, m_{e} is the electron mass, c is the speed of light, $n_{\mathrm{e}}(\theta)$ is again the number density of electrons and $T_{\mathrm{e}}(\theta)$ is the temperature of the electrons. Note that this equation does not include z—the effect is redshift independent. Relativistic corrections to this equation can be found in e.g. Itoh et al. (1998).

The SZ effect is related to a detectable flux density S at frequency ν by

$$S_\nu = \frac{2\nu^2 k_{\mathrm{B}} T_{\mathrm{CMB}}}{c^2} f(x) \int y(\theta) d\Omega, \tag{3}$$

where the integral is over the observed section of sky and $f(x) = x^2 e^x g(x)/(e^x - 1)^2$ represents the frequency dependence of the effect, in which $g(x) = (x/\tanh(x/2)) - 4$ and the dimensionless frequency $x = h\nu/k_{\mathrm{B}}T_{\mathrm{CMB}}$. T_{CMB} is the present-day temperature of the CMB.

The SZ effect has a major advantage with locating clusters compared to optical and X-ray detections in that the magnitude of the effect does not depend on redshift, and as such it should be possible to observe clusters of galaxies out to high redshifts relatively easily. Additionally, the SZ effect only depends on n_e, not n_e^2 as in X-ray, so the outer part of the cluster atmosphere can also be observed (see Figure 3), and less complications will arise from substructure and cooling/heating effects within the cluster (Motl et al., 2005).

Only the thermal SZ effect is considered here. A kinetic SZ effect also exists; see section 5 of the review by Birkinshaw (1999). Depending on the velocity of the cluster relative to the CMB, this may be important.

3 Virtual skies

There are several ways of creating simulations of the large scale structure of the universe. Most common are N-body simulations; these are generally used for looking at the distributions of clusters (e.g. Retzlaff et al., 1998; Evrard et al., 2002) and their evolution over time. As a result, they can provide expected mass functions and number counts, e.g. Jenkins et al. (2001). Additionally, they can be used to investigate the distribution of dark matter within haloes.

Additional detail can be simulated by adding hydrodynamical simulations to N-body simulations. These consist of solving the hydrodynamical equations with various physical effects, such as radiative cooling, adiabatic compression and shock heating, and are therefore useful for simulating the distributed material such as the intracluster medium (see e.g. Muanwong et al., 2002).

Virtual cluster catalogues can be obtained from these simulations, which can then be used directly to create maps by applying models of clusters at each cluster position; for a recent example of this, see Schäfer et al. (2006). However, there are a limited number of these catalogues available due to the amount of computing power required for each simulation; for example, the gigaparticle (10^9) simulation run by Evrard et al. (2002) took around 7 months to run on a 512-CPU computer. An alternative approach is to use theoretical equations calibrated by the simulations to create similar maps comparatively easily and much quicker; this is the approach used here. Additional sources, for example the CMB, can be added to the maps in both cases by using information from other programs.

Creation of the virtual sky maps falls neatly into three parts—first, the cosmology, which covers the CMB and the distribution of galaxy clusters in the sky; second, the simulation of each cluster and third, the various foregrounds. These parts are dealt with sequentially within this section. An outline of the process is given in Appendix B.

3.1 Cosmology

The fiducial cosmology used here is ΛCDM, i.e. with present day values for the matter densities of $\Omega_{\mathrm{m}} = 0.3$ (of which $\Omega_{\mathrm{b}} = 0.019/h_{100}^2$), $\Omega_\Lambda = 0.7$, $\Omega_{\mathrm{r}} = \Omega_{\mathrm{k}} = 0$, and $h_{100} = 0.70$ (where the Hubble constant $H_0 = 100 h_{100}$ km s^{-1} Mpc^{-1}) and $\sigma_8 = 0.9$. These parameters are easily changeable to allow for the investigation of different cosmologies.

3.1.1 Cosmic Microwave Background

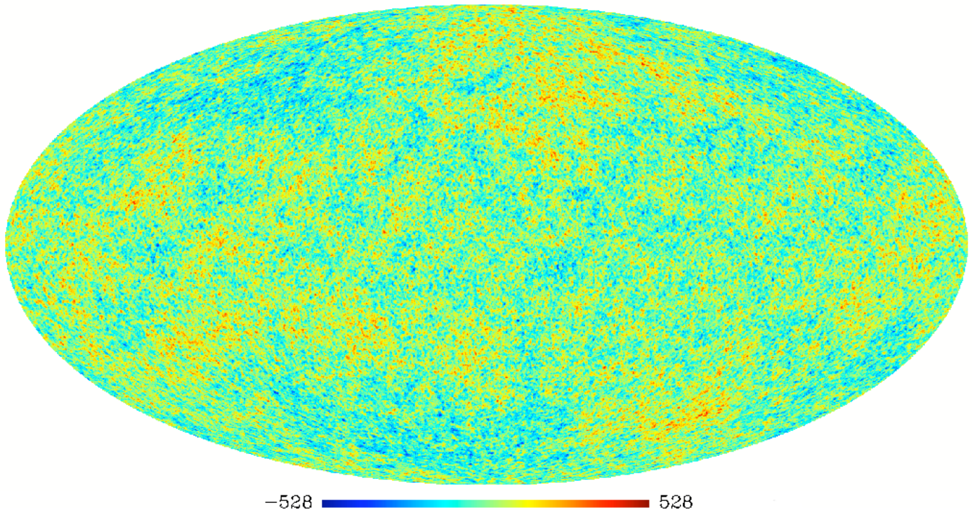

Figure 4: A realization of the CMB generated from CAMB and equations 4–7. The scale is in μk

The CMB is added into the map using a power spectrum (a set of C_l's) generated by CAMB (Lewis et al., 2000). Assuming that the CMB has a gaussian distribution (i.e. the power spectrum contains all of the information about the CMB), the C_l's can be converted to a random set of complex spherical harmonic coefficients (a_{lm}'s) via

$$\Re(a_{lm}) = \sqrt{-2\ln(\alpha) C_l}\cos(2\pi\beta), \tag{4}$$

$$\Im(a_{lm}) = 0 \tag{5}$$

for $m = 0$, and

$$\Re(a_{lm}) = \sqrt{-\ln(\alpha) C_l}\cos(2\pi\beta), \tag{6}$$

$$\Im(a_{lm}) = \sqrt{-\ln(\alpha) C_l}\sin(2\pi\beta) \tag{7}$$

for $1 \leq m < l$, with the maximum value of l being established by the resolution of the map. α and β are random variables, the value of which is computed separately for each value of m and l. The coefficients for negative values of m can be found by $a_{l,-m} = a_{l,m}*$, where * denotes complex conjugation. The $a_{l,m}$'s can then be converted to create a map via a fourier transform; see Figure 4 for an example of the result.

3.1.2 Distribution of galaxy clusters

The positions of galaxy clusters can be specified in three dimensions—θ and ϕ on the sky, and the redshift z. To these, a fourth parameter needs to be added—the mass of the cluster—to fully specify the distribution. These four parameters are then used as the input parameters for a cluster model.

Mass and redshift

The dependence of the number of clusters with z is given by

$$\frac{dN}{dz} = \Delta\Omega \frac{dV}{dz d\Omega}(z) \int_{M_{\rm lim}(z)}^{\infty} \frac{dN}{dM}(M, z) dM, \tag{8}$$

where $\Delta\Omega$ is the solid angle of the sky being looked at, $\frac{dN}{dM}(M, z)$ is the comoving number density of clusters with mass M and redshift z and $M_{\rm lim}(z)$ is the minimum mass that is being considered (this is usually the minimum detectable mass size). This can easily be adapted to give the number of clusters in a given mass range.

$$\frac{dV}{dz d\Omega} = \frac{r(z)^2}{H(z)} = \frac{\left(\int_0^z H^{-1}(z')dz'\right)^2}{H(z)} \tag{9}$$

is the comoving volume in a flat universe, in which $r(z)$ is the coordinate distance. $H(z)$ is the Hubble parameter, which is given by the Friedmann equation

$$E(z)^2 = \frac{H^2(z)}{H_0^2} = \Omega_{\rm m}(1+z)^3 + \Omega_{\rm r}(1+z)^4 + \Omega_{\rm k}(1+z)^2 + \Omega_\Lambda. \tag{10}$$

The standard Press-Schechter mass function is (Press & Schechter, 1974)

$$\frac{dN}{dM}(z, M) = -\sqrt{\frac{2}{\pi}} \frac{\rho_{\rm m}(t_0)}{M} \frac{\delta_{\rm c}}{D(z)\sigma(M)^2} \frac{d\sigma(M)}{dM} \exp\left(-\frac{\delta_{\rm c}^2}{2D(z)^2\sigma(M)^2}\right), \tag{11}$$

in which $\delta_{\rm c} = 1.686$, $\rho_{\rm m}(t_0)$ is the present value of the matter density and $\sigma(M)$ is the current over-density with mass M; this can be calculated from the density power spectrum. $D(z)$ is the growth factor, which is normalized by $D(0) = 1$; the dependence on redshift can be found by solving the perturbation equation for matter fluctuations (see Battye & Weller, 2003). This can be calibrated by N-body simulations; Evrard et al. (2002) provide an equation for the mass function at $z = 0$, which can be generalized in redshift to give

$$\frac{dN}{dM}(z, M_{200}) = -A \frac{\rho_{\rm m}(t_0)}{M_{200}\sigma(M_{200})} \frac{d\sigma(M_{200})}{dM} \exp[-|B - \ln[D(z)\sigma(M_{200})]|^\epsilon], \tag{12}$$

where M is the cluster mass within an overdensity of 200 (see §3.2.1), A, B and ϵ are parameters that can be found by fitting to the simulation. They provide values for these parameters for both ΛCDM and τCDM ($\Omega_{\rm m} = 1, \Omega_\Lambda = 0$) cosmologies. To account for $\Omega_{\rm M}$ varying with redshift in ΛCDM, where it approaches 1 at high redshifts, they interpolate between the two sets of parameters by

$$A(\Omega_{\rm m}(z)) = (1-x)A(\tau{\rm CDM}) + xA(\Lambda{\rm CDM}), \tag{13}$$

with $x = (1-\Omega_{\rm m}(z))/0.7$, using similar equations for B and ϵ.

The value for $\sigma(M)$ can be calculated in several different ways. Battye & Weller (2003) calculate it directly using a spherical top hat window function and the linear power spectrum, which is based upon the transfer function; this is calculated using CMBFAST (Seljak & Zaldarriaga, 1996). Alternatively, a parameterized equation can be used. The one from Evrard et al. (2002) is used here; this states that

$$\ln\sigma^{-1}(M_{200}) = -\ln\sigma_{15} + a\ln M_{200} + b(\ln M_{200})^2, \tag{14}$$

where $\ln\sigma_{15} = \ln\sigma_8 + {\rm const.}$, which is 0.578 for $\sigma_8 = 0.9$, and for ΛCDM the parameters $a = 0.281$ and $b = 0.0123$. M_{200} is the mass of the cluster within an overdensity of 200 in units of $10^{15}h^{-1}M_\odot$.

The total number of clusters on a map of a given size $\Delta\Omega$ on the sky can be found by integrating equation 8 over both mass and redshift; to make the map more realistic, this number can then be Poisson distributed. A 2D probability distribution can be formed by calculating equation 8 for different mass and redshift ranges; a catalogue of individual cluster masses and redshifts can then be obtained by using a random number generator to sample from this probability distribution.

Distribution on the sky

The simplest method of positioning clusters on the sky is to Poisson distribute them, i.e. by generating the positions from a random distribution. However, this will not create the clustering of the clusters that is expected from theory and N-body simulations.

There are several sources of this clustering. First, early galaxy clusters are formed at peaks in the density fluctuations set up by quantum fluctuations in the early universe; this will impart a specific distribution upon them. This is most important with the distribution of high-mass clusters, which will have subsequently evolved approximately linearly with time via gravity. Second, clusters will gravitationally attract each other in a non-linear way. This is more important with smaller clusters or groups than large ones, as they will tend to cluster around the larger clusters. The third, and most complicated, source of clustering is due to mergers and close encounters between clusters.

N-body and hydrodynamical simulations generally contain at least some of the sources of clustering. Figure 5 shows a cluster map using a catalogue from one of the Hubble Volume Simulations (Evrard et al., 2002), and the same map but with the positions randomized (effectively removing the clustering). It can be seen that the first is more clumpy, with some voids where there are few clusters, while the second is much more uniform; this is the result of clustering.

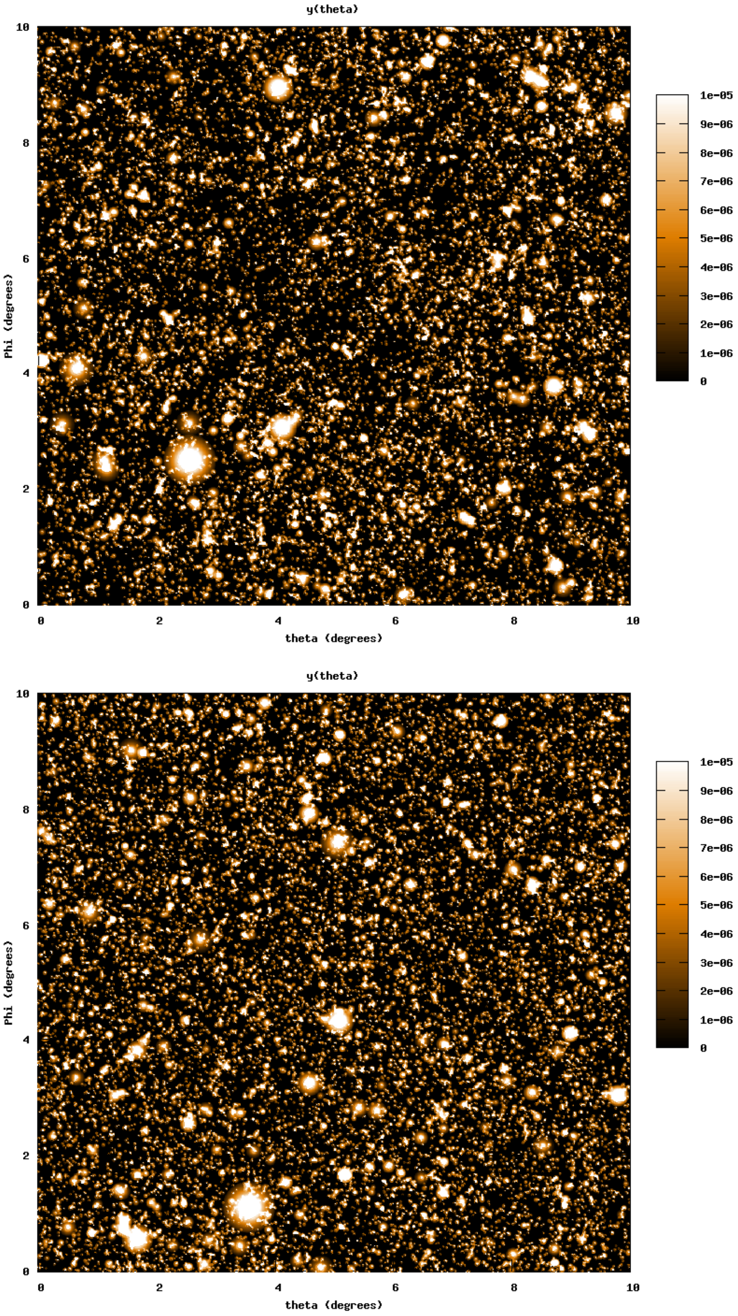

Figure 5: Maps of the compton y parameter using the Virgo Consortium Hubble Volume Simulation ΛCDM Deep Wedge cluster catalogue (Evrard et al., 2002) and the cluster model described in §3.2. Top: using the unaltered cluster catalogue (i.e. clustered). Bottom: randomizing the positions of the clusters on the sky (i.e. no clustering). Note the over- and under-dense areas on the top map, whereas the bottom map is more uniform. The maps have been saturated to show the fainter detail; the true maximum value is $y = 1.6 \times 10^{-5}$.

3.2 Galaxy cluster model

Creating a simplistic, spherically symmetric model of a cluster requires several components. Given an input mass and redshift, the radius and average density need to be found. The density of both the gas and the dark matter at different radii can then be calculated using density profiles. Finally, the temperature of the gas needs to be calculated. Combined, these specify the size and shape of the SZ effect and X-ray emission expected from a cluster.

3.2.1 Gravitational collapse

The virial radius r_{vir} of the cluster can be calculated by using a spherical infall model (see e.g. Peebles, 1980). This gives

$$r_{\mathrm{vir}} = \left(\frac{3M_{\mathrm{vir}}}{4\pi\Delta_{\mathrm{c}}\rho_{\mathrm{crit}}} \right)^{1/3}, \tag{15}$$

where M_{vir} is the virial mass of the cluster. ρ_{crit} is the critical density for the universe to have a closed topology; it is given by

$$\rho_{\mathrm{crit}}(z) = \frac{3H(z)^2}{8\pi G}, \tag{16}$$

in which $H(z)$ is the Hubble parameter, as given by equation 10, and G is the gravitational constant. Δ_{c} is the overdensity of the cluster at the virial radius, defined as

$$\Delta_{\mathrm{c}} = \frac{\rho_{\mathrm{cluster}}}{\rho_{\mathrm{crit}}}. \tag{17}$$

The value for Δ_{c} depends on the cosmological parameters; in an Einstein-de Sitter universe, this is exactly $18\pi^2 \approx 178$ (Komatsu & Seljak, 2001). Bryan & Norman (1998) provide a fitting formula for cases where $\Omega_{\mathrm{R}} = 0$;

$$\Delta_{\mathrm{c}} = 18\pi^2 + 82(\Omega_{\mathrm{m}}(z) - 1) - 39(\Omega_{\mathrm{m}}(z) - 1)^2, \tag{18}$$

where $\Omega_{\mathrm{m}}(z) = \Omega_{\mathrm{m}}(1+z)^3/E^2(z)$ (cf. equation 10).

The radius at which the cluster has an overdensity of 200 can also be calculated, via

$$r_{200} = \left(\frac{3M_{200}}{4\pi 200\rho_{\mathrm{crit}}} \right)^{1/3}, \tag{19}$$

and similarly for other overdensity values.

These radii can be converted to an angular size on the sky via dividing them by the angular distance measure, e.g. $\theta_{\mathrm{vir}} = r_{\mathrm{vir}}/d_{\mathrm{A}}(z)$, where

$$d_{\mathrm{A}}(z) = \frac{\int_0^z H^{-1}(z')dz'}{(1+z)}. \tag{20}$$

3.2.2 Density profiles

The spherical profiles that are used to describe the distribution of matter within clusters are generally of the form (Suto et al., 1998):

$$\xi\left(x\right)=\frac{1}{x^{\alpha}\left(1+x^{\delta}\right)^{\gamma}},\tag{21}$$

where $x=r/r_{\rm s}$ and α, δ and γ are dimensionless parameters. This profile provides a central core, and inner and outer power-law slopes. $r_{\rm s}$ is a critical radius that describes the turn-over point between the core and the power-law slope, commonly called the core radius. It is defined as $r_{\rm s}=r_{\rm vir}/c$, where c is a concentration parameter. The profile can be truncated at the virial radius $r_{\rm vir}$, which prevents potential divergence in the gas mass (e.g. Birkinshaw, 1999; Battye & Weller, 2003).

Gas profile

Setting $\alpha=0$, $\delta=2$, $\gamma=\frac{3\beta}{2}$ into (21) gives the well-known β profile

$$\xi\left(x\right)=\frac{1}{\left(1+x^{2}\right)^{\frac{3\beta}{2}}},\tag{22}$$

which was originally found by fitting to X-ray observations (Cavaliere & Fusco-Femiano, 1976). It has since been found to be related to hydrostatic equilibrium (see e.g. Makino et al., 1998; Lancaster et al., 2004). It generally gives a good fit to the gas profile in the inner part of clusters. This can be related to the number density of electrons by

$$n_{\rm e}(x)=n_{\rm e0}\xi(x),\tag{23}$$

where $n_{\rm e0}$ represents the electron density at the core of the cluster.

Equation 22 can be projected from 3D to a 2D sky to become (Battye & Weller, 2003)

$$\zeta_{\rm ICM}(\varphi)=\left(1+\varphi^{2}\right)^{\frac{1}{2}-\frac{3\beta}{2}}\frac{J\left(\left(\frac{c^{2}-\varphi^{2}}{1+\varphi^{2}}\right)^{1/2},\beta\right)}{J(c,\beta)},\tag{24}$$

where

$$J(a,b)=\int_{0}^{a}\left(1+x^{2}\right)^{-\frac{3b}{2}}dx\tag{25}$$

and $\varphi=\theta/\theta_{\rm s}$, in which $\theta_{\rm s}=r_{\rm s}/d_{\rm A}$ and θ is the angular distance from any given position in the sky to the center of the cluster. Value of $c=10$ and $\beta=2/3$ are used, following Battye & Weller (2003).

Dark matter profile

Setting $\alpha = 1$, $\delta = 1$, $\gamma = 2$ into (21) gives the NFW profile (Navarro et al., 1997; see also §2 of Ostriker et al., 2005), namely:

$$\xi\left(x\right) = \frac{1}{x\left(1+x\right)^2}. \tag{26}$$

This was found by fitting profiles to dark matter halos from N-body/hydrodynamical simulations run by Navarro et al. (1995, 1996, 1997), and is now the profile of choice for modeling dark matter halos. It can be related to the dark matter density profile by

$$\rho(x) = \rho_{\rm crit}\Delta_{\rm c}\xi(x). \tag{27}$$

Equation 26 can be projected onto a 2D sky to become (Bartelmann, 1996)

$$\zeta_{\rm DM}(\varphi) = \frac{2}{\varphi^2-1}\begin{cases} 1-\frac{2}{\sqrt{\varphi^2-1}}\arctan\left(\sqrt{\frac{\varphi-1}{\varphi+1}}\right) & \varphi > 1 \\ 1-\frac{2}{\sqrt{1-\varphi^2}}\arctan\left(\sqrt{\frac{1-\varphi}{1+\varphi}}\right) & \varphi < 1 \\ 1 & \varphi = 1 \end{cases}. \tag{28}$$

Values for the concentration parameter vary; see Eke et al. (2001) for a compilation. Here, we assume a constant value of $c = 5$.

The central surface density of a cluster can be calculated by (Ostriker et al., 2005)

$$\Sigma_0 = \frac{M_{\rm vir}}{2\pi r_s^2(\ln(1+c)-(c/(1+c)))}. \tag{29}$$

The surface density at distance $\varphi = \theta/\theta_{\rm s}$ from the center of the cluster is then

$$\Sigma(\varphi) = \Sigma_0\zeta_{\rm DM}(\varphi). \tag{30}$$

3.2.3 Mass–Temperature Relationship

The simplest model of a cluster would consist of purely gravitational effects, where the gas in the cluster gravitationally collapses with a release of energy into heat given by the Virial theorem. Assuming that the cluster is isothermal, this is given by (Birkinshaw, 1999)

$$k_{\rm B}T_{\rm e} \approx \frac{GMm_{\rm p}}{2r_{\rm vir}} \approx 7\left(\frac{M}{3\times10^{14}M_\odot}\right)\left(\frac{r_{\rm vir}}{\rm Mpc}\right)^{-1}\ {\rm keV}. \tag{31}$$

Battye & Weller (2003) introduce an "electron density weighted average temperature" by $\langle T_{\rm e}\rangle_{\rm n} = \int n_{\rm e}T_{\rm e}dl/\int n_{\rm e}dl$. By assuming that clusters are in thermal equilibrium, are virialized (hence the Virial Theorem can be applied) and that virialization only involves gravitational heating, the following equation is deduced for a universe containing dark energy:

$$\langle T_{\rm e}\rangle_n = T_*\left(\Delta_{\rm c}E(z)^2\right)^{1/3}\left(1+(1+3w)\frac{\Omega_{\rm Q}(z)}{\Delta_{\rm c}}\right)(1+z)^{\varepsilon-1}\left(\frac{M_{\rm vir}}{10^{15}h^{-1}M_\odot}\right)^{1/\xi}, \tag{32}$$

in which $M_\odot$ is the solar mass and the dimensionless parameters $\varepsilon = 1$ and $\xi = 3/2$. T_* is a normalization factor, the calculated value of which is 0.5; however, the authors point out that both observed and simulated clusters point to a T_* between 1.0 and 2.2. Following them, we adopt a value of 1.6 here.

$\Omega_{\rm Q}$ is the ratio of dark energy to the critical density of the universe; they use a quintessence model, which is a function of z. w is the equation of state for the dark energy, given by P_Q/ρ_Q. We use $w = -1.0$ and $\Omega_Q = \Omega_\Lambda = 0.7$.

The authors suggest that the value for ξ "could model non-gravitational heat input", and that ε "models deviations from complete virialization". Suggested values are $1.48 \leq \xi \leq 1.98$, with no preference for the value of ε. These parameters are kept as their standard values here.

Using equation 32, the SZ decrement at any point can then be calculated by

$$y(\theta) = \frac{\langle T_{\rm e}\rangle_{\rm n}}{m_{\rm e}} \tau_0 \zeta_{\rm IGM} \left(\frac{\theta}{\theta_{\rm s}}\right), \tag{33}$$

in which τ_0 is the central optical depth of the cluster. This is given by (Battye & Weller, 2003)

$$\tau_0 = \frac{\sigma_{\rm T}}{d_{\rm A}^2} \frac{f_{\rm gas} M_{\rm vir}}{\mu_{\rm e} m_{\rm p}} \frac{1}{\int \zeta(\theta/\theta_{\rm s}) d\Omega}, \tag{34}$$

where $f_{\rm gas} = 0.12$ is the ratio of the matter in the intracluster medium to the total mass of the cluster ($M_{\rm vir}$), $\mu_{\rm e} = 1.143$ is the mean mass per electron and $m_{\rm p}$ is the proton mass. The integral is over the entire cluster.

$y(\theta)$ can then be converted to a temperature change in the CMB via

$$\Delta T(\theta) = y(\theta) g(x) T_{\rm CMB} \tag{35}$$

where $g(x)$ is as defined in §2.3.

3.3 Point sources

Point sources are astrophysical sources that are not resolved at the scale of the map (which is typically ~ 1 arcminute here), excluding CMB anisotropies and clusters. Two types of point sources are considered here. Radio point sources, which include AGN, synchrotron and free-free emission, are dominant at low frequencies. At high frequencies, infrared sources become important; these are dusty, high redshift galaxies.

3.3.1 Flux density distribution

Various experiments and theoretical calculations provide values for dN/dS, the differential source counts as a function of flux density, for the different types of point sources. This can be used to obtain the total number of point sources with a flux density between $S_{\rm min}$ and $S_{\rm max}$ in an area $\Delta\Omega$ on the sky by

$$N_{\rm tot} = \beta \Delta\Omega \int_{S_{\rm min}}^{S_{\rm max}} \frac{dN}{dS_\nu} dS_\nu. \tag{36}$$

β can be used as an enrichment factor to account for any increase in the number of point sources in a particular direction. The flux densities of individual sources can then be calculated by randomly sampling from a probability distribution defined by a normalized dN/dS between the flux density limits.

The point source flux densities can be converted to effective temperatures using

$$T = \frac{S_\nu}{\theta^2_{\text{pixel}} \frac{dB}{dT}}, \tag{37}$$

where θ^2_{pixel} is the area of the pixel containing the point source, and

$$\frac{dB}{dT} = \frac{2k}{c^2} \left(\frac{kT_{\text{CMB}}}{h} \right)^2 \frac{x^4 e^x}{(e^x - 1)^2}, \tag{38}$$

is the differential of the Planck function with respect to temperature. Once more, x is the dimensionless frequency, given by $x = h\nu / k_{\text{B}} T_{\text{CMB}}$.

Radio sources

The dN/dS of radio sources can be parameterized by a single power law of the form

$$\frac{dN}{dS_\nu} = \frac{N_0}{S_0} \left(\frac{S_\nu}{S_0} \right)^{-\alpha}. \tag{39}$$

Cleary et al. (2004) provide a fit to observations by the VSA, at 33GHz where $S_0 = 70$mJy, $\alpha = 2.34^{+0.25}_{-0.26}$ and $N_0/S_0 = 10.6^{+2.3}_{-2.2}$ mJy^{-1}sr^{-1}. They provide a rescaling factor for the Toffolatti et al. (1998) model (henceforth T98) of 0.68; this rescaled T98 model is used here. The T98 model allows for a varying power law. This avoids Olber's paradox occurring at low flux densities; the VSA power law gives an increasing number of sources at low flux densities), hence the large difference between the VSA power law and the T98 model apparent in Figure 6.

The flux densities are scaled to the desired frequency ν by a power law, $S_\nu / S_{30\text{GHz}} = (\nu/30\text{GHz})^\alpha$ with a value for α that is gaussianly distributed about a mean of $\overline{\alpha} = -0.3$, with $\sigma_\alpha = 0.36$, for each source. Figure 7 shows the flux density distribution resulting from the rescaling to 8.4GHz of a point source map created using the T98 model at 30GHz; this agrees with the observational data taken at 8.4GHz that is also plotted.

Infrared sources

Infrared sources can be parameterized using a double power law of the form

$$\frac{dN}{dS_\nu} = \frac{N_0}{S_0} \left[\left(\frac{S}{S_0} \right)^\alpha + \left(\frac{S}{S_0} \right)^\beta \right]. \tag{40}$$

Borys et al. (2003) suggest that the parameters at 350GHz should be $S_0 = 1.8$mJy, $\alpha = 1.0$, $\beta = 3.3$ and $N_0 = 1.5 \times 10^4$ deg^{-2}. Following White & Majumdar (2003), this is extrapolated to different frequencies using $S_\nu = \nu^\gamma$, where $\gamma = 2.5$.

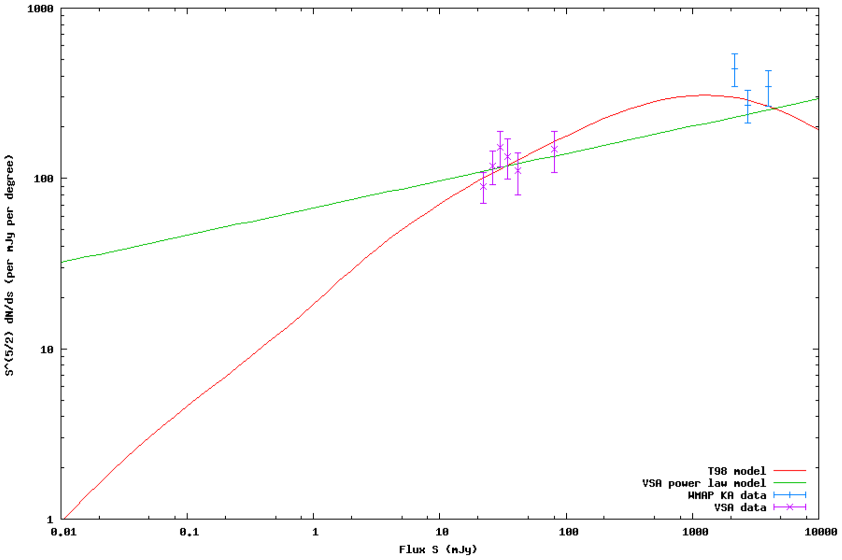

Figure 6: Differential point source number count as a function of flux density. Plotted are the T98 model at 30GHz (red line; Toffolatti et al., 1998), the VSA power law (green line; see equation 39) and data from the VSA (purple, Cleary et al., 2004) and WMAP (blue, Bennett et al., 2003), both at 33GHz.

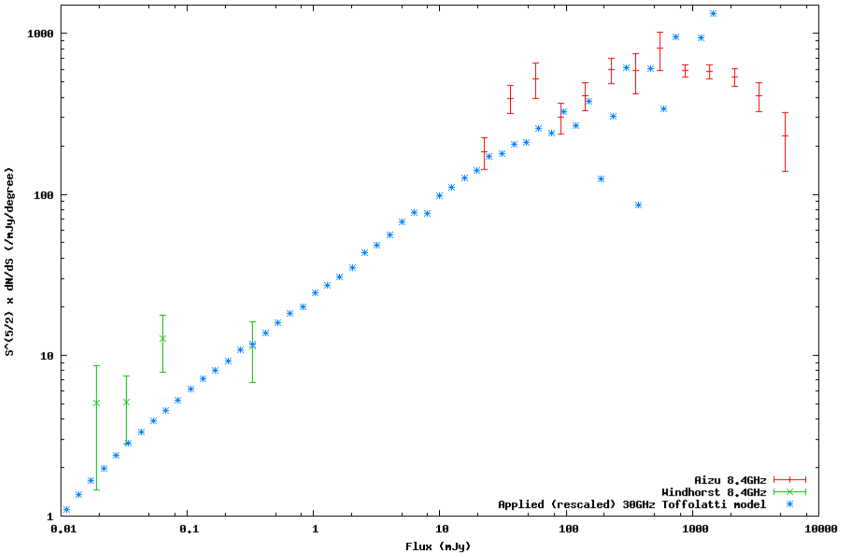

Figure 7: Differential point source number count as a function of flux density at 8.4GHz. Blue points are from a realization of point sources in an 8.4GHz virtual sky map, extrapolated from the 30GHz T98 model; the large scatter at high flux densities is due to small number statistics. Red data points are from 10GHz observations by Aizu et al. (1987), rescaled to 8.4GHz by Windhorst et al. (1993); green data points are at 8.4GHz from Windhorst et al. (1993).

3.3.2 Spatial distribution

The sources are spatially distributed in two ways. One method is to simply distribute them randomly over the map, so that the probability of finding a source at a particular position, $P(x, y)$, is constant across the map. The second method is to distribute them according to the surface density $\Sigma(x, y)$ of the cluster to some power, here 1/3, in which case

$$P(x, y) = \frac{(\Sigma(x, y))^{1/3}}{\int_{x,y} \Sigma(x, y)\, dx\, dy}. \tag{41}$$

As the radio point sources are thought to reside in galaxies within clusters, these are distributed according to the surface density, and their number is enriched by a factor of 3 when a single cluster is being mapped. Infrared sources, however, are at high redshift, and any clustering present in their distribution will be unrelated to the galaxy cluster. Thus, they are not enriched and are randomly distributed.

Figure 9 shows the effect of distributed, enriched radio point sources and randomly distributed infrared sources on the SZ effect from a simulated large, nearby cluster.

3.3.3 Power spectra

Figure 8 shows the effect of point sources on the power spectra of the sky. Also plotted are the CMB and SZ power spectra; it can be seen that the point sources dominate over these at high values of l. As such, the high flux point sources need to be subtracted off before the power spectra can be measured.

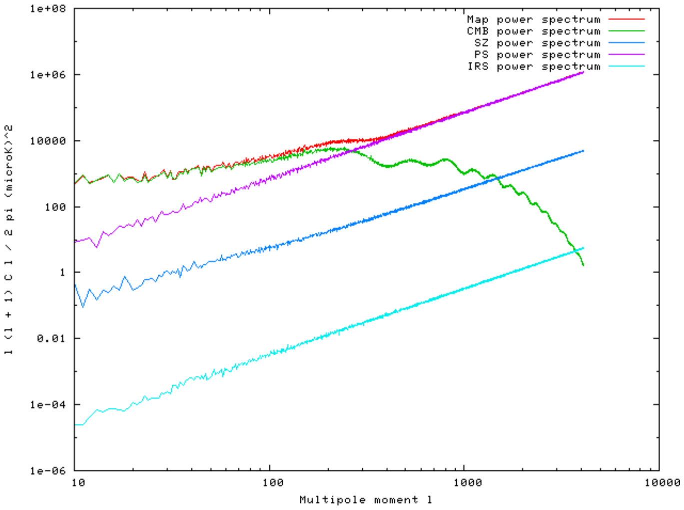

Figure 8: Power spectra of the different components of the Virtual Sky model at 30GHz up to $l = 4096$; the CMB (green), SZ effect (blue), radio point sources (purple) and infrared point sources (turquoise); the combined power spectra is in red.

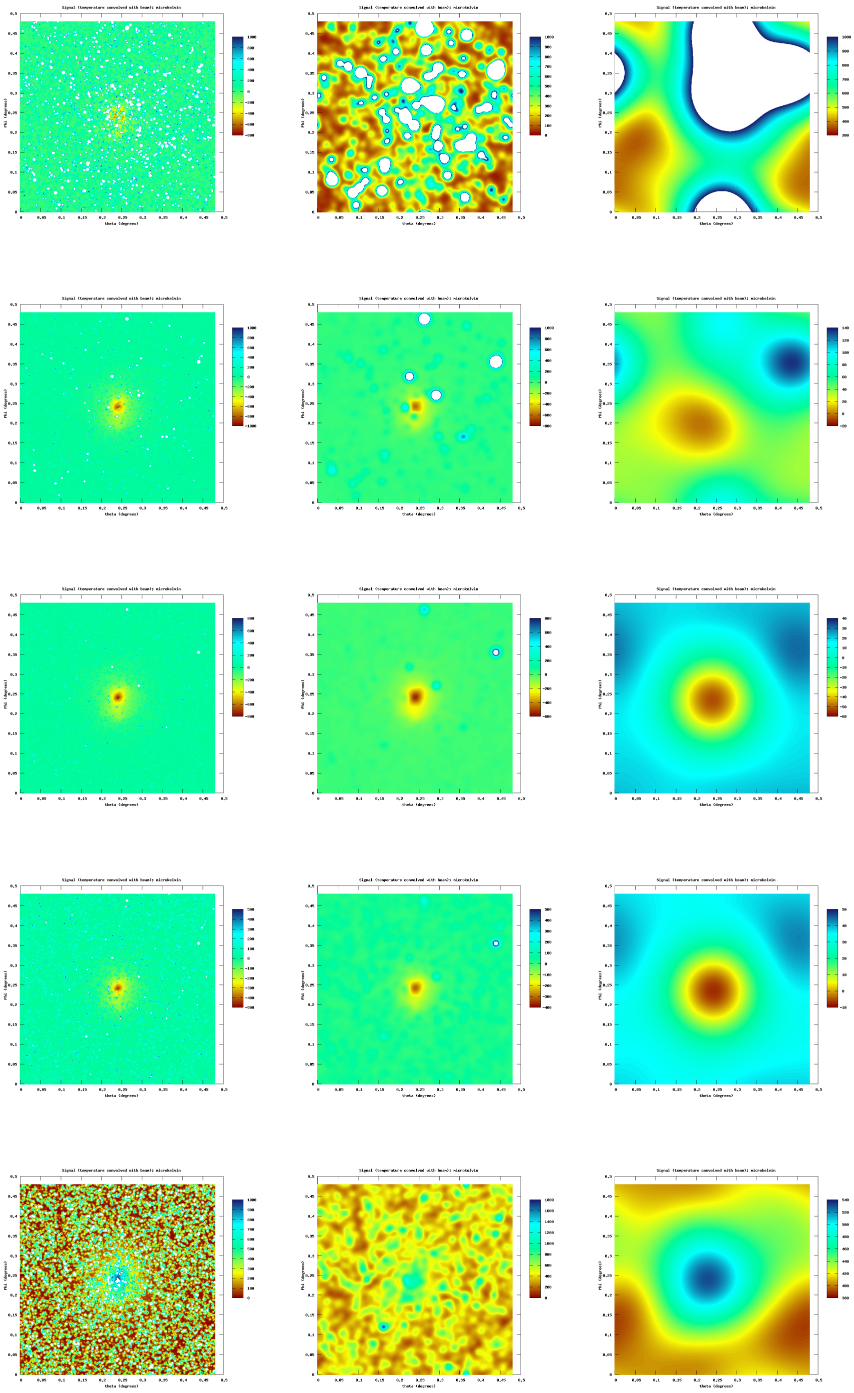

Figure 9: Point source contamination of a $10^{15}h^{-1}M_{\odot}$ cluster from Kay et al. (2004), positioned at $z = 0.2$. Enriched and distributed radio sources, as well as random infrared sources, are present. Across: beam size (12 arcseconds, 1 arcminutes, 10 arcminutes). Down: frequency (10, 30, 90, 150, 350GHZ)

4 Future work

This section aims to give a rough guide to the future progression of this work in both the short and long term. It should not be regarded as a definite plan; it will most likely be affected by work done by other parties, as well as interesting directions for the work that arise and other events outside the author's control.

4.1 Improving the virtual sky

All of the components of the virtual sky can be further investigated and improved upon to make them more realistic; however, the majority of the components are now at a stage where they can be considered good enough to be used to obtain scientific results (see §4.2). The components that need to be added in or improved upon in the near future include:

- The CMB is currently only added to all-sky maps; ideally, it should also be applied to the flat sky maps.
- It is expected that Brightest Cluster Galaxies, which lie at or near to the center of clusters, are more likely to be radio loud than normal galaxies (see e.g. Best et al., 2006; Magliocchetti & Bruggen, 2007). This needs to be researched and added to the virtual sky model.
- A way to add the expected instrumental noise per pixel to the maps needs to be constructed.

In the more long term, potential improvements include:

- Using more realistic models for individual clusters (the current model is described in §3.2). For examples of alternative models, see Ostriker et al. (2005) and Komatsu & Seljak (2001).
- Further improvements can be made to the point source distribution within clusters of galaxies, specificially with the enrichment as a function of distance from the center (see e.g. Coble et al., 2006).
- Use could be made of Pinnochio (Monaco et al., 2002) to create galaxy cluster catalogues much more quickly than N-body techniques; the output from this could then be used as inputs to the virtual sky in place of the $dN/dz(z, M)$ function and random spatial positioning. This would allow an investigation into the clustering of galaxy clusters.

4.2 Science outputs from virtual skies

Estimates of confusion noise

Confusion can arise between the SZ effect from clusters of galaxies and intrinsic CMB fluctuations; each is a noise source to the other. This presents problems with detecting clusters by the SZ effect; the signal can either be hidden or amplified by the background CMB fluctuations (Lancaster et al., 2004). Also, at frequencies lower than 217GHz (the turnover point of the SZ effect), point sources can fill parts of the SZ decrement, either distorting it or hiding it completely. At large angular scales, cluster-cluster confusion can also be present, meaning that while a cluster is detected, it cannot be properly identified.

These effects need to be quantified so that they can be corrected for within real data. Using a virtual sky to do this is ideal as the inputs are known and can be compared with the output from analysis to obtain the detection efficiency, corrections for the measurements, et cetera.

Algorithms for extracting clusters

Various methods exist to detect clusters amidst the CMB fluctuations and point sources. Multi-frequency observations can distinguish between different objects (the CMB, clusters and point sources) by looking at their spectral dependency; alternatively, objects appearing as point sources in a single frequency map can be removed. More advanced methods include filtering (see e.g. Vale & White, 2005; Schäfer et al., 2006) and bayesian statistics (Diego et al., 2002). These algorithms can be tested and compared using virtual sky maps, allowing their efficiency to be characterized as well as their mis-identification rate.

Initial work will focus on trialling tools such as Source Extractor (Bertin & Arnouts, 1996) to see how well they can seperate SZ clusters and point sources, as well as creating catalogues of each.

Planck simulations

The Planck Surveyor is a space mission that will be launched in the next few years and should be able to detect thousands of clusters through the SZ effect (see e.g. Geisbuesch & Hobson, 2006). Virtual skies for the different frequencies and resolutions of Planck are shown in Figure 10. Using these maps and the different techniques for extracting clusters, Planck's ability to detect clusters can be assessed and optimized.

CBI excess

The Cosmic Background Imager (CBI) is an interferometer observing between 26 and 36GHz since 1999 (see Padin et al., 2002, for the technical details). In 2003, the discovery of an excess in the CMB power spectrum at high multipoles ($l = 2000 - 3500$) by the instrument was announced (Mason et al., 2003). This is currently believed to be due

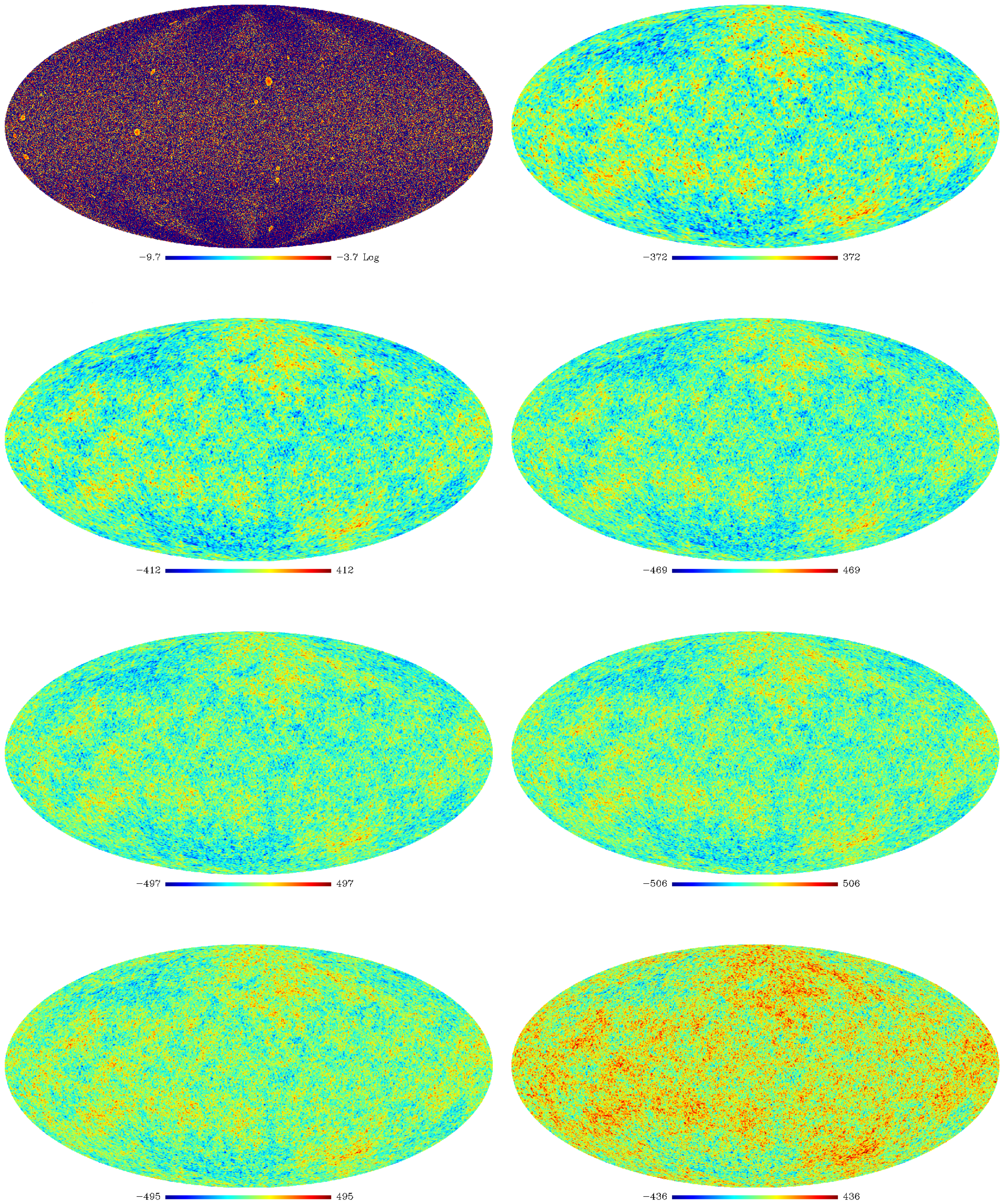

Figure 10: Top left: an all-sky logarithmic Compton $y(\theta)$ map. The other maps are (from top to bottom, left to right) 30, 44, 70, 100, 143, 217 and 353GHz virtual sky maps consisting of the CMB, galaxy clusters (using the distribution in the top-left map) and radio and infrared point sources. The frequencies represent Planck observing frequencies; the maps have been smoothed to the appropriate beam sizes in each case (33, 24, 14, 9.5, 7.1, 5.0 and 5.0 arcminutes respectively).

to the SZ effect (Bond et al., 2005). By creating a large number of virtual skies and analysing their power spectra, the probability for this to occur can be quantified and the effect in general investigated.

Using an UMBRELLA

In order to get the best results from real observations, the observational methods and instrument noise first need to be well understood. Lowe (2006) has constructed a computer simulation (an Upper Millimeter Band Receiver Emulator for Large Linked Arrays, or UMBRELLA for short) of the OCRA-p instrument (see §4.3) and the atmosphere, and has thus far only used this to do mock observations of point sources. This software can be modified to observe the virtual skies described above; it can then be used to do mock observations of SZ clusters.

It should also be possible to modify the software to simulate the more complex OCRA-F instrument; once this is done, then it could be used to trial blind surveys to find the best observing methods. This would also enable the quantification of the detection efficiency of clusters with different masses and redshifts using the instrument. As an additional bonus, a computer program to reduce the data and turn it into a map will be required; once this has been constructed and tested using virtual simulations it can be used on real data.

4.3 Observing with OCRA-F

The One Centimeter Reciever Array (OCRA) is a three-stage project with the ultimate goal of constructing a 100-beam receiver at 30GHz (1cm), to be positioned at the secondary focus of a large parabolic radio telescope (Browne et al., 2000). The first stage was a 2-beam prototype (OCRA-p), which has been observing on the 32m telescope at Toruń, Poland, for the last few years (Lowe, 2006). This instrument has been used to observe point sources (the CJF sample; see Lowe, 2006 and Lowe et al., 2007), and has made some initial observations of clusters through the SZ effect (Lancaster et al., 2007).

OCRA-F (Faraday) is a 16 beam prototype that is nearing completion (Figure 11 shows the instrument as it was in April 2007); it should be mounted on the Toruǹ telescope around April 2008. This instrument will be eight times quicker than OCRA-p, due to the increase in the number of horns, and will also be able to observe a larger area of the sky at any one time. This makes it a useful survey instrument.

There are several interesting astrophysical questions that can be answered by surveying using OCRA-F. Observations of point sources in the field to the mJy level would allow them to be better characterized, making them easier to remove from other observations and also to calculate how many clusters will be lost as a result of their presence. The enrichment of point sources towards clusters is also of interest; recent difficulties have been encountered by groups searching for the SZ effect in nearby ($z < 0.5$) clusters, which have yet to be definitively explained and could be due to this enrichment towards clusters.

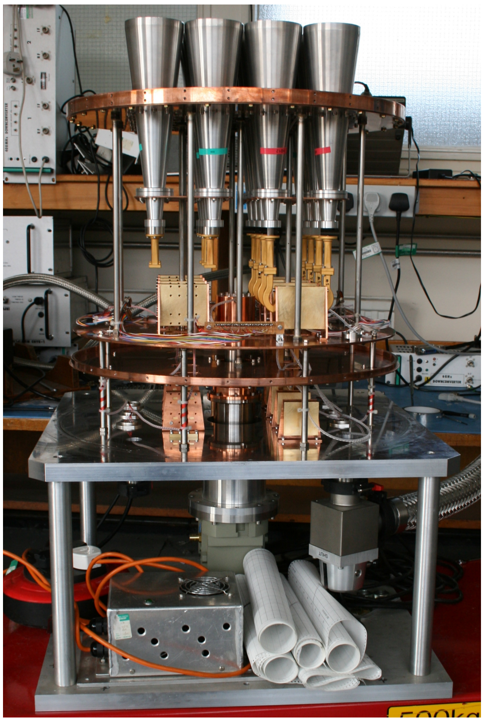

Figure 11: The OCRA-F receiver.

The ultimate aim for OCRA-F would be to conduct blind surveys for SZ clusters; not many attempts have been made at this by other groups, and only a couple of new clusters have been discovered this way to date.

5 Conclusions

The work done so far has mostly been to familiarize the author with the subject area, as well as to create a bespoke program that can generate cosmological maps of the sky. To a large extent, this work is not new; similar work has been done using slightly different methods in the past. However, it has set the stage for work to be done in the future that has not yet been accomplished by other people.

Acknowledgments

I am grateful for the guidance provided by my supervisors, Professor Ian Browne and Dr. Richard Battye, and the many useful conversations held with Professor Peter Wilkinson, Dr. Scott Kay and Dr. Stuart Lowe. I am also indebted to PPARC (now known as STFC) for funding my postgraduate studies.

Appendices

A Map making

A.1 Pixelisation

Two methods of pixelizing the maps are used here. For small areas of the sky, the small angle approximation means that a simple cartesian grid can be used to pixelize a flat sky. For larger (>30 degrees across) areas of the sky, this cannot be assumed. In this case, we use HEALPix (Hierarchical Equal Area isoLatitude Pixelization; Górski et al., 2005), which pixelises a sphere in such a way that the area in each pixel is constant and the pixels all lie on the same latitude. The resolution of the map is determined by the value of $N_{\rm side}$, which must be a power of 2; the total number of pixels is then $N_{\rm pix} = 12N_{\rm side}^2$ and the area of each pixel is $4\pi/N_{\rm pix}$.

A.2 Convolution with a gaussian beam

A gaussian beam generally has a quoted Full Width at Half Maximum (FWHM); this can then be converted into a standard deviation σ via

$$\sigma = \frac{\theta_{\rm FWHM}}{\sqrt{8\ln 2}} \tag{42}$$

The normalized beam power at a distance r from the center of the beam can then be calculated by

$$P(x) = \frac{1}{\sqrt{2\pi}\sigma}\exp(-r^2/2\sigma^2) \tag{43}$$

A brute force method of carrying out the convolution is to create a map of the beam at the same resolution as the sky map, appropriately normalized (i.e. such that the sum of all pixels in the map is equal to 1), and then center this map at each pixel in the sky map, carry out a matrix multiplication, then add the results into the corresponding pixel on the convolved map. This works well for situations where the beam map is much smaller than the sky map, however it takes a long time where this is not the case.

A much quicker method is to fourier transform the sky map, then multiply this by the fourier transform of the beam,

$$P(k) = \exp(-k^2\sigma^2/2), \tag{44}$$

where $k = 2\pi/\theta_{\rm map}$, in which $\theta_{\rm map}$ is the width of the map, before fourier transforming the map back into real space. In this situation, the size of the beam has no impact on the speed of the convolution. This is the method now used within the virtual sky program, with FFTW (Frigo & Johnson, 2005) used to carry out the fourier transforms.

B Program outline

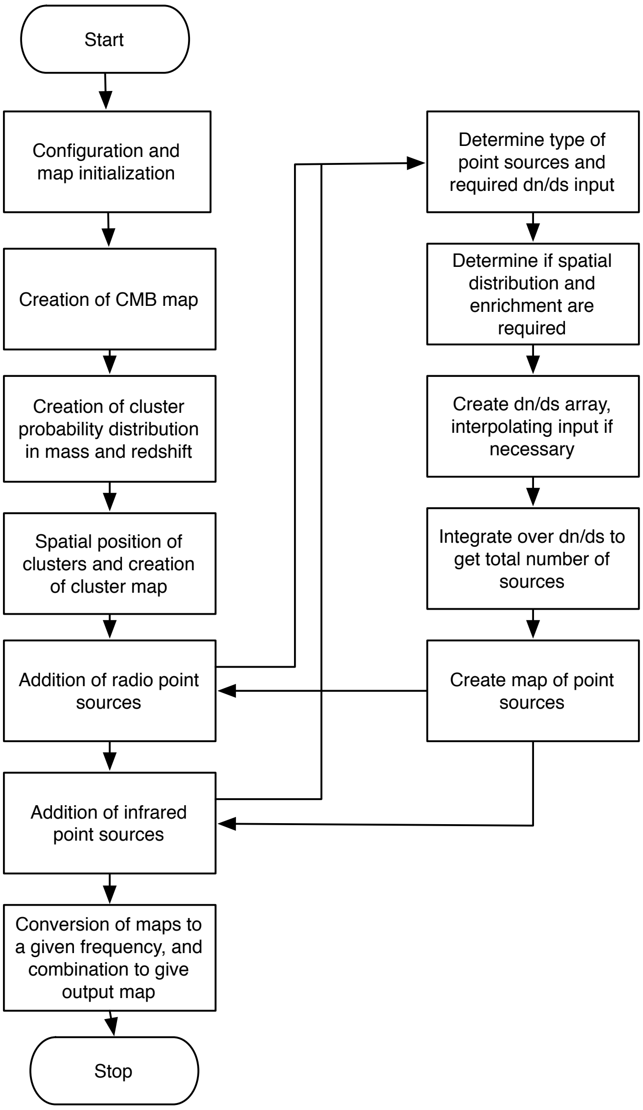

Figure 12: An outline of the steps involved in creating a virtual sky

References

Abell, G. O. 1958. The Distribution of Rich Clusters of Galaxies. ApJS, 3, 211

Abell, G. O., Corwin, Jr., H. G., & Olowin, R. P. 1989. A catalog of rich clusters of galaxies. ApJS, 70, 1

Aizu, K., Inoue, M., Tabara, H., & Kato, T. 1987, in IAU Symposium, Vol. 124, Observational Cosmology, ed. A. Hewitt, G. Burbidge, & L. Z. Fang, 565–+

Bartelmann, M. 1996. Arcs from a Universal Dark-Matter Halo Profile. A&A, 313, 697

Battye, R. A., & Weller, J. 2003. Constraining cosmological parameters using Sunyaev-Zel'dovich cluster surveys. Phys. Rev. D, 68, 083506

Bennett, C. L. et al. 2003. First-Year Wilkinson Microwave Anisotropy Probe (WMAP) Observations: Foreground Emission. ApJS, 148, 97

Bertin, E., & Arnouts, S. 1996. Sextractor: Software for source extraction. Astronomy and Astrophysics Supplement Series, 117, 393

Best, P. N., von der Linden, A., Kauffmann, G., Heckman, T., & Kaiser, C. 2006. On the prevalence of radio-loud AGN in brightest cluster galaxies: implications for AGN heating of cooling flows. arXiv:astro-ph/0611197v2

Birkinshaw, M. 1999. The Sunyaev-Zel'dovich Effect. Phys. Rep., 310, 97

Biviano, A. 2000, in Constructing the Universe with clusters of galaxies, astro-ph/0010409

Bond, J. R. et al. 2005. The Sunyaev-Zel'dovich Effect in CMB-calibrated Theories Applied to the Cosmic Background Imager Anisotropy Power at l > 2000. ApJ, 626, 12

Borys, C., Chapman, S., Halpern, M., & Scott, D. 2003. The HDF-North SCUBA Super-map I: Submillimetre maps, sources and number counts. MNRAS, 344, 385

Browne, I. W., Mao, S., Wilkinson, P. N., Kus, A. J., Marecki, A., & Birkinshaw, M. 2000. OCRA: a One-Centemeter Receiver Array. Proc. SPIE, 4015

Bryan, G. L., & Norman, M. L. 1998. Statistical Properties of X-Ray Clusters: Analytic and Numerical Comparisons. ApJ, 495, 80

Carlstrom, J. E., Joy, M., & Grego, L. 1996a. Interferometric Imaging of the Sunyaev-Zeldovich Effect at 30 GHz. ApJ, 456, L75

——. 1996b. Interferometric Imaging of the Sunyaev-Zeldovich Effect at 30 GHz: Erratum. ApJ, 461, L59

Cavaliere, A., & Fusco-Femiano, R. 1976. X-rays from hot plasma in clusters of galaxies. A&A, 49, 137

Cleary, K. A. et al. 2004. Source subtraction for the extended Very Small Array and 33-GHz source count estimates. astro-ph/0412605

Clewley, L., van Breukelen, C., & Bonfield, D. 2006. Detecting galaxy clusters at $0.1 < z < 2.0$. astro-ph/0612118

Coble, K., Carlstrom, J. E., Bonamente, M., Dawson, K., Holzapfel, W., Joy, M., LaRoque, S., & Reese, E. D. 2006. Radio Point Sources Toward Galaxy Clusters at 30 GHz. astro-ph/0608274

De Lucia, G. et al. 2004. The Buildup of the Red Sequence in Galaxy Clusters since z ˜ 0.8. ApJL, 610, L77

Diego, J. M., Vielva, P., Martínez-González, E., Silk, J., & Sanz, J. L. 2002. A bayesian non-parametric method to detect clusters in planck data. MNRAS, 336, 1351

Eke, V. R., Navarro, J. F., & Steinmetz, M. 2001. The Power Spectrum Dependence of Dark Matter Halo Concentrations. ApJ, 554, 144

Evrard, A. E. et al. 2002. Galaxy Clusters in Hubble Volume Simulations: Cosmological Constraints from Sky Survey Populations. ApJ, 573, 7

Frigo, M., & Johnson, S. G. 2005. The Design and Implementation of FFTW3. Proceedings of the IEEE, 93, 216

Geisbuesch, J., & Hobson, M. 2006. Cosmology with the Planck cluster sample. astro-ph/0611567

Gladders, M. D., & Yee, H. K. C. 2000. A New Method For Galaxy Cluster Detection. I. The Algorithm. AJ, 120, 2148

Górski, K. M., Hivon, E., Banday, A. J., Wandelt, B. D., Hansen, F. K., Reinecke, M., & Bartelmann, M. 2005. HEALPix: A Framework for High-Resolution Discretization and Fast Analysis of Data Distributed on the Sphere. ApJ, 622, 759

Itoh, N., Kohyama, Y., & Nozawa, S. 1998. Relativistic Corrections to the Sunyaev-Zeldovich Effect for Clusters of Galaxies. ApJ, 502, 7

Jenkins, A., Frenk, C. S., White, S. D. M., Colberg, J. M., Cole, S., Evrard, A. E., Couchman, H. M. P., & Yoshida, N. 2001. The mass function of dark matter haloes. MNRAS, 321, 372

Jones, C., & Forman, W. 1999. Einstein Observatory Images of Clusters of Galaxies. ApJ, 511, 65

Kay, S. T., Thomas, P. A., Jenkins, A., & Pearce, F. R. 2004. Cosmological simulations of the intracluster medium. MNRAS, 355, 1091

Komatsu, E., & Seljak, U. 2001. Universal gas density and temperature profile. MNRAS, 327, 1353

Lancaster, K. et al. 2007. Preliminary Sunyaev Zel'dovich Observations of Galaxy Clusters with OCRA-p. MNRAS, (online early), arXiv:0705.3336v1 [astro-ph]

——. 2004. Very Small Array observations of the Sunyaev-Zel'dovich effect in nearby galaxy clusters. MNRAS, 359, 16

Lewis, A., Challinor, A., & Lasenby, A. 2000. Efficient computation of CMB anisotropies in closed FRW models. ApJ, 538, 473

Lowe, S. 2006, PhD thesis, Jodrell Bank, University of Manchester

Lowe, S. et al. 2007. (in prep)

Magliocchetti, M., & Bruggen, M. 2007. The interplay between radio galaxies and cluster environment. arXiv:0705.0574v1 [astro-ph]

Makino, N., Sasaki, S., & Suto, Y. 1998. X-ray gas density profile of clusters of galaxies from the universal dark matter halo. ApJ, 497

Mason, B. S. et al. 2003. The Anisotropy of the Microwave Background to l = 3500: Deep Field Observations with the Cosmic Background Imager. ApJ, 591, 540

Monaco, P., Theuns, T., Taffoni, G., Governato, F., Quinn, T., & Stadel, J. 2002. Predicting the Number, Spatial Distribution and Merging History of Dark Matter Haloes. ApJ, 564, 8

Motl, P. M., Hallman, E. J., Burns, J. O., & Norman, M. L. 2005. The Integrated Sunyaev-Zeldovich Effect as a Superior Method for Measuring the Mass of Clusters of Galaxies. ApJ, 623, L63

Muanwong, O., Thomas, P. A., Kay, S. T., & Pearce, F. R. 2002. The effect of cooling and preheating on the X-ray properties of clusters of galaxies. MNRAS, 336, 527

Navarro, J. F., Frenk, C. S., & White, S. D. M. 1995. Simulations of X-ray clusters. MNRAS, 275, 720

——. 1996. The Structure of Cold Dark Matter Halos. ApJ, 462, 563

——. 1997. A Universal Density Profile from Hierarchical Clustering. ApJ, 490, 493

Oegerle, W. R., & Hill, J. M. 2001. Dynamics of cD Clusters of Galaxies. IV. Conclusion of a Survey of 25 Abell Clusters. AJ, 122, 2858

Ostriker, J. P., Bode, P., & Babul, A. 2005. A Simple and Accurate Model for Intra-Cluster Gas. ApJ, 634, 964

Padin, S. et al. 2002. The cosmic background imager. PASP, 114, 83

Peebles, P. J. E. 1980, The Large-Scale Structure of the Universe (Princeton University Press)

Press, W. H., & Schechter, P. 1974. Formation of Galaxies and Clusters of Galaxies by Self-Similar Gravitational Condensation. ApJ, 187, 425

Retzlaff, J., Borgani, S., Gottloeber, S., Klypin, A., & Mueller, V. 1998. Constraining cosmological models with cluster power spectra. New Astronomy, 3, 631

Schäfer, B. M., Pfrommer, C., Bartelmann, M., Springel, V., & Hernquist, L. 2006. Detecting Sunyaev-Zel'dovich clusters with Planck - I. Construction of all-sky thermal and kinetic SZ maps. MNRAS, 370, 1309

Schäfer, B. M., Pfrommer, C., Hell, R. M., & Bartelmann, M. 2006. Detecting Sunyaev-Zel'dovich clusters with Planck - II. Foreground components and optimized filtering schemes. MNRAS, 370, 1713

Seigar, M. S., Graham, A. W., & Jerjen, H. 2006. Intracluster light and the extended stellar envelopes of cD galaxies: An analytical description. astro-ph/0612229

Seljak, U., & Zaldarriaga, M. 1996. A Line-of-Sight Integration Approach to Cosmic Microwave Background Anisotropies. ApJ, 469, 437

Sunyaev, R. A., & Zeldovich, Y. B. 1970. Small-Scale Fluctuations of Relic Radiation. Astrophysics and Space Science, 7, 3

——. 1972. The Observation of Relic Radiation as a Test of the Nature of X-Ray Radiation from the Clusters of Galaxies. Comments on Astrophysics and Space Physics, 4, 173

Suto, Y., Sasaki, S., & Makino, N. 1998. Gas density and X-Ray surface brightness profiles of clusters of galaxies from dark matter halo potentials: beyond the isothermal β model. ApJ, 509, 544

Toffolatti, L., Argueso Gomez, F., de Zotti, G., Mazzei, P., Franceschini, A., Danese, L., & Burigana, C. 1998. Extragalactic source counts and contributions to the anisotropies of the cosmic microwave background: predictions for the Planck Surveyor mission. MNRAS, 297, 117

Vale, C., & White, M. 2005. Finding Clusters in SZ Surveys. New Astronomy, 11, 207

Weymann, R. 1966. The Energy Spectrum of Radiation in the Expanding Universe. ApJ, 145, 560

White, M., & Majumdar, S. 2003. Point Sources in the context of future SZ surveys. astro-ph/0308464

Windhorst, R. A., Fomalont, E. B., Partridge, R. B., & Lowenthal, J. D. 1993. Microjansky source counts and spectral indices at 8.44 GHz. ApJ, 405, 498

York, D. G. et al. 2000. The Sloan Digital Sky Survey: Technical Summary. AJ, 120, 1579

Zeldovich, Y. B., & Sunyaev, R. A. 1969. The interaction of matter and radiation in a hot-model universe. Astrophysics and Space Science, 4, 301